university of groningen

faculty of science and engineering

Simulation of superficial neuromast inspired flow sensor

An integration Project submitted in fulfilment of the requirements for the degree of Bachelor of Industrial Engineering and Management

Author: Ivan Orlov s3905993
1st Supervisor: Dr. A. Kottapalli
2nd Supervisor: M. Mohebbi
Daily Supervisor: Dr. D. Sengupta
June 16, 2023

I. ABSTRACT

This report covers all the steps required for conducting a flow sensor simulation study. First, a problem context explains the inspiration for the sensor working principle, attempts by other researchers at creating similar sensors, and the sensor design at hand. Four sensor designs, one cylindrical and three ellipsoids with different ratios between the minor and major axes, are made into 3D models using COMSOL software by closely following the supervisor's requirements for the sensor geometry. Next, an FSI simulation is set up with the sensor, made out of PDMS, positioned inside a tube of flowing water. Two tests, investigating various flow velocities and angles, are configured. A mesh optimization study revealed that coarser mesh density settings offered the best trade-off between the accuracy and speed of the simulation. The simulations are computed using a segregated approach. Data about tip displacement, stress, and inner tube elongation were extracted from the simulations and presented in the form of plots and images using COMSOL tools and some additional derivations. Finally, all the obtained results were discussed in light of the performance criteria defined in the problem context. The key findings of the research are as follows. Thinner sensors reach higher tip displacement but saturate earlier, hence more suitable for slower flow velocities. A larger difference between width and thickness leads to a higher degree of directionality in sensor behavior and also increases the stress and inner tube deformation. An ellipsoid 1:3 is proposed as the best among tested shapes. It exhibited the highest tip displacement, stress, and inner tube deformation, all of which are desirable as they increase the likelihood of the real-world sensor producing measurable output.

CONTENTS

II. ABBREVIATIONS

- Lateral Line System - LLC
- Superficial Neuromast - SN
- Canal Neuromast - CN
- Polydimethylsiloxane - PDMS

III. INTRODUCTION

Throughout history, engineers have been captivated by the endless ingenuity of nature when it comes to developing sensing mechanisms. From the intricate compound eyes of insects to the finely tuned sonar systems of dolphins, the natural world has consistently inspired engineers to look for better sensor designs. By studying and emulating the elegant solutions found in nature, engineers have successfully developed a wide range of sensors with never-before-imagined accuracy and size.

One such inspiration is a lateral line system(LLS) found in most aquatic vertebrates. This organ consists of tiny sensing units called neuromasts. While being no larger than seven millimeters, with some being as small as ten micrometers (Montgomery, Windsor, and Bassett 2009), neuromasts can detect water acceleration as small as 0.1 mm/s^2 (Netten 2005). Besides being highly sensitive and compact, neuromasts are also multi-functional. Their functionality consists of detecting fluid velocity around the fish body, sensing disturbances in the water, and filtering out background noises (M. J. McHenry, Strother, and Netten 2008). All of the aforementioned advantages are highly desirable when creating artificial sensors.

Although such a sensor can be used wherever fluid movement detection is required, some of the most promising use cases include swarm robots sensing mechanism (Bernoulli Institute for Mathematics and Intelligence 2021) and sensing critical flows associated with intravenous infusions (Kottapalli, Shen, et al. 2017). As shown by review papers written by Wang et al. (2021) and Bora et al. (2018), there have been many attempts at creating the neuromast-inspired sensor with ever-increasing success. Nevertheless, there is still a long way before engineers can reach the high sensing mechanisms standards set by nature.

Modern technologies allow engineers to test many designs without ever producing the sensor by creating numerical models and conducting simulations. This project explores four sensor shapes, which are inspired by the superficial neuromasts found in nature. The sensor performance is accessed by creating 3D models and conducting fluid-structure interaction(FSI) simulations. The results are analyzed to determine areas of stress concentration and sensor body deformation under various fluid flow velocities and angles. All the findings will aid future researchers determine the best shape for an artificial neuromast-inspired sensor.

IV. PROBLEM CONTEXT AND SYSTEM DESCRIPTION

A. Lateral Line system

The LLS is a primitive sensory system found in aquatic vertebrates, including fish and amphibians. It allows these organisms to detect and perceive mechanical disturbances in the water, serving as a vital "touch at a distance" sense. The system consists of specialized mechanosensory organs known as neuromasts, which play a crucial role in various behaviors such as spatial orientation, prey detection, predator avoidance, and perception of static obstacles (Netten 2005).

The LLS comprises two main types of neuromasts: superficial neuromast (SN) and canal neuromasts (CN). Superficial neuromasts are

located on the surface of the animal's skin, protruding into the surrounding water, while canal neuromasts are positioned below the skin surface within fluid-filled canals. Both types of neuromasts consist of sensory hair cells and a gelatinous cupula that covers them (Windsor and M. McHenry 2009). The schematic overview of neuromast components can be found in figure 1.

SN and CN serve distinct functions and possess unique structural features. SN has an elongated cupula and functions as cantilevered beams with flexible tips. When SN undergoes deformation due to the water flow, the bending of the cupula transfers mechanical information to the underlying mechanosensory hair cells. A system model of the SN working principle can be found in figure 2. SN is involved in detecting local near-field water motion, such as those produced by prey or predators, and plays a role in behaviors like obstacle detection and mating. In contrast, CN is recessed within canals beneath the scales and possesses a hemispherical cupula. The cupula behaves as a rigid body that slides along the epithelium when pushed by water flow. CN primarily detects changes in water pressure and is sensitive to the different frequencies when compared to SN (M. J. McHenry and Netten 2007) (Montgomery, Windsor, and Bassett 2009).

B. Neuromast inspired sensors

Wang et al. (2021) and Bora et al. (2018) in their papers performed a comprehensive overview of existing bio-inspired sensors. There have been proposed several different sensor designs and most of them use piezoresistive material as a sensing mechanism. The general
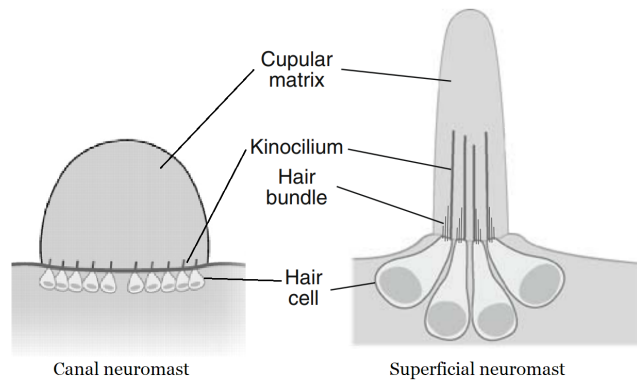

Fig. 1: Schematic overview of the CN and SN, not to scale. Both neuromasts contain a cupular matrix that covers kinocilium attached to hair cells. Picture adapted form M. J. McHenry, Strother, and Netten (2008)

Fig. 2: The system model of the SN. When the neuromast gets displaced by the water flow, it causes the kinocilium inside to move, which stimulates the hair cells and sends signals to the nervous system. The displacement is affected by cupula properties like shape, size, orientation, and material (Windsor and M. McHenry 2009).

working principle of these sensors can be summarized as follows: When the water pressure is applied, the sensor body gets deformed, which causes a proportional change in resistance that can be measured. This project is focused on sensors developed by the advanced production engineering research group. The simplified sensor schematics can be found in figure 3. The sensor design consists of a cupula made of Polydimethylsiloxane (PDMS). Inside the

cupula, there is a vertical tube. The tube is filled with a liquid and left to dry. After all the liquid evaporates, a thin layer of piezoresistive material remains on the tube wall. When the cupula experience deformation, the stress inside the tube will change the conductivity of the piezoresistive material. The piezoresistive material is deposited as a thin layer on the inside of an empty tube and does not have a significant effect on the structural properties of the overall sensor, so the tube can be modeled as if it is empty.
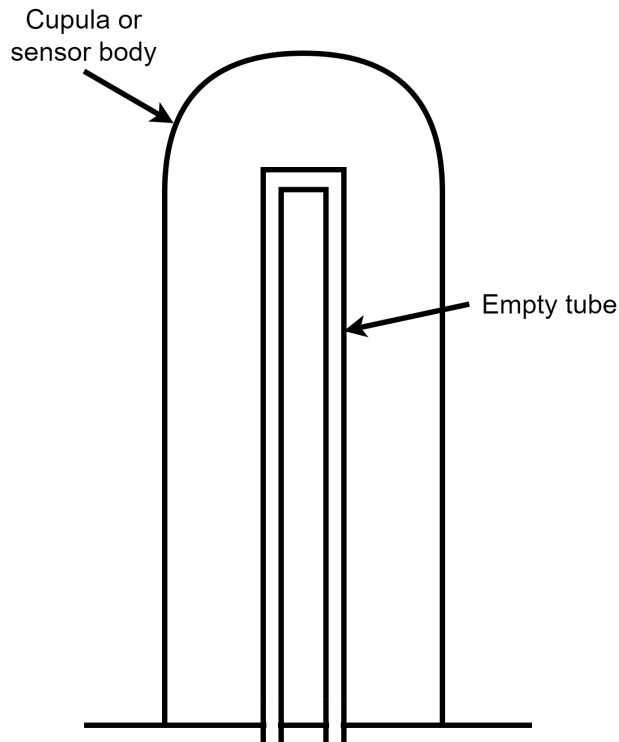
Fig. 3: The simplified sensor schematics consist of a sensor cupula and an empty tube. Different sensor cupula shapes will be considered during the research.

C. Tools

The primary tool of this project is a simulation. It plays a crucial role in the design and construction of a sensor because it allows engineers to predict and evaluate the sensor's performance and behavior in various scenarios without the need for physical prototypes or costly experimentation. The neuromast detects fluid movement by deforming, thus requiring the use of FSI simulation. FSI simulation is a computational technique that examines the dynamic relationship between fluid flow and flexible solid structures, allowing for an understanding of how they influence each other's behavior. During the planning stage of this research, two main simulation software were considered: ANSYS and COMSOL. Both software supports FSI simulation and all the physics required for it. The ANSYS software is frequently used when studying the dynamics of cardiovascular systems (Saeedi, Shamloo, and Mohammadi 2019)(Shamloo, Nejad, and Saeedi 2017). With the approval of the first supervisor the COMSOL software was chosen due to two main reasons. First, it is available in the IT service provided by the University of Groningen. Second, it was used in the earlier projects conducted by the APE research group.

D. Sensor performance criteria

An important question to ask is how can a sensor's performance be measured? In other words, what are the criteria for deciding how the sensor's body shape performs when compared to the other sensors? Other studies about artificial sensors are looking at what minimum and maximum deformation can be registered by measuring the sensor output voltage (Wissman et al. 2019) (McConney et al. 2009) (Kottapalli, Bora, et al. 2016) (Peleshanko et al. 2007), which is heavily dependent on the sensing

mechanism and sensor production. Since the physical prototype is out of the scope of this project, another approach is required.

As mentioned earlier, the sensing mechanism is based on a piezoresistive material, which means that a higher strain will result in higher output from the sensor. The simplest way to determine which sensor experiences higher strain is by measuring the tip displacement. A greater tip displacement indicates higher sensor deformation and a better chance of being measurable in real-world tests. However, the change in tip displacement is also important, because if the sensor has the same tip displacement for different fluid velocities, it is likely that the output of the sensor will also be the same, rendering the sensor useless. A desirable sensor would have a linear relationship between input and output with a high rate of change.

Another parameter that can be measured is the elongation of the inner tube. The strain experienced by the piezoresistive material should be the same as the strain of the inner tube, so a higher absolute value of inner tube elongation is desirable.

Lastly, strain is directly linked to the stress experienced by the object. Higher stress inside the sensor body is beneficial, as it will yield a higher output compared to a sensor with minimal internal stress.

E. Research objective and questions

The research objective of this project is to find the correlation between sensor body shape and performance by creating the FSI simulation in COMSOL and conducting two main tests: The effect of water flow velocity on tip displacement, stress inside the sensor body, and inner tube elongation; The effect of water flow angle on tip displacement, stress inside the sensor body, and inner tube elongation. The test results should aid the development of the sensor by suggesting the sensor's body shape for sensing small-scale fluid flows.

The main research question is:

1) How does the shape of the sensor body affect the sensor performance under various fluid flow conditions?

The research sub-questions are:

1) What is the right procedure for creating a sensor 3D model?
2) What are the simulation settings for the required tests?
3) What is the structural behavior of the sensor under various flow conditions?

The last sub-question can be further split into the following questions that directly link to the tests performed during the research

   a) What is the cupula tip displacement under different flow velocities?
   b) What is the stress in the sensor body under different flow velocities?
   c) What is the inner tube elongation under different flow velocities?
   d) What is the cupula tip displacement under different flow directions?
   e) What is the stress in the sensor body under different flow directions?
   f) What is the inner tube elongation under different flow directions?

The first two research sub-questions are answered in the section V. The last research sub-question is answered in the section VI. The central research question of this project is answered in the section VII

8

A. 3D model

The following section describes in detail the modeling process of the sensor 3D model. All the model requirements such as shape and size were provided by the supervisor. There are 4 main cupula shapes investigated in this project: one cylindrical and three ellipsoid shapes with 1:1, 1:2, and 1:3 ratios between their major and minor axes. All the modeling is done using the COMSOL software. The building steps of each sensor feature are organized into separate groups to improve the simulation readability and make it modification-friendly.

The first feature is the sensor body. An ellipsoid is created and the bottom half of it is removed. The 1:1 ellipsoid has a width and a thickness of $0.03[mm]$. The 1:2 ellipsoid has a width of $0.03[mm]$ and a thickness of $0.015[mm]$. The 1:3 ellipsoid has a width of $0.045[mm]$ and a thickness of $0.015[mm]$. Next, a cuboid base with a height of $0.025[mm]$ and a side of $0.2[mm]$ is created below the ellipsoid. To create a cylindrical shape, an additional feature is added where a cylinder of height $0.245[mm]$ and a diameter of $0.03[mm]$ is created. This feature is suppressed if the ellipsoid is required, otherwise, both the ellipsoid and cylinder are created and merged into one shape. Since an ellipsoid will be always contained within a cylinder of the same thickness and width, only the cylinder remains. The model is configured in such a way as to avoid creating separate files for cylindrical and ellipsoid sensors. Suppressing the creation of an ellipsoid for the cylindrical sensor is also not an option, because then the program will treat those ob-

jects as different geometries and future merging and subtracting operations would have to be configured manually each time the sensor is changed from cylindrical to ellipsoid or vice versa. Next, a semi-sphere is placed on top of the cylinder with the same diameter. The final sensor cupula height is $0.275[mm]$.

The second feature is the inner tube. The tube remains the same for each sensor shape. First, two vertical cylinders are created $0.02[mm]$ away from each other with a height of $0.175[mm]$ and a diameter of $0.0150[mm]$. The tube has the same diameter throughout its shape. A half-torus is created above the cylinders with a major radius of $0.01[mm]$ and a minor radius of $0.0075[mm]$. The torus is merged with the two cylinders. Next, two horizontal cylinders are created on each side starting a the base edge and ending just below each vertical cylinder. The cylinders are connected to the rest of the geometry using a quarter torus with the same major and minor radii. Finally, the obtained geometry is subtracted from the sensor body to create an inner tube. Figure 4 contains images of the geometry building tree and building steps for an ellipsoid 1:2 sensor

Figure 5 contains the picture of the finished sensor models. Each sensor cupula has a version with additional canals and one without additional canals. The original sensor design, without the additional canals, encountered difficulties during the manufacturing process. After the sensor body is 3D printed, the inner tube is filled with piezoresistive liquid without any air pockets to make a continuous layer of piezoresistive material. Initially, one side of the tube was used as an inlet and the other
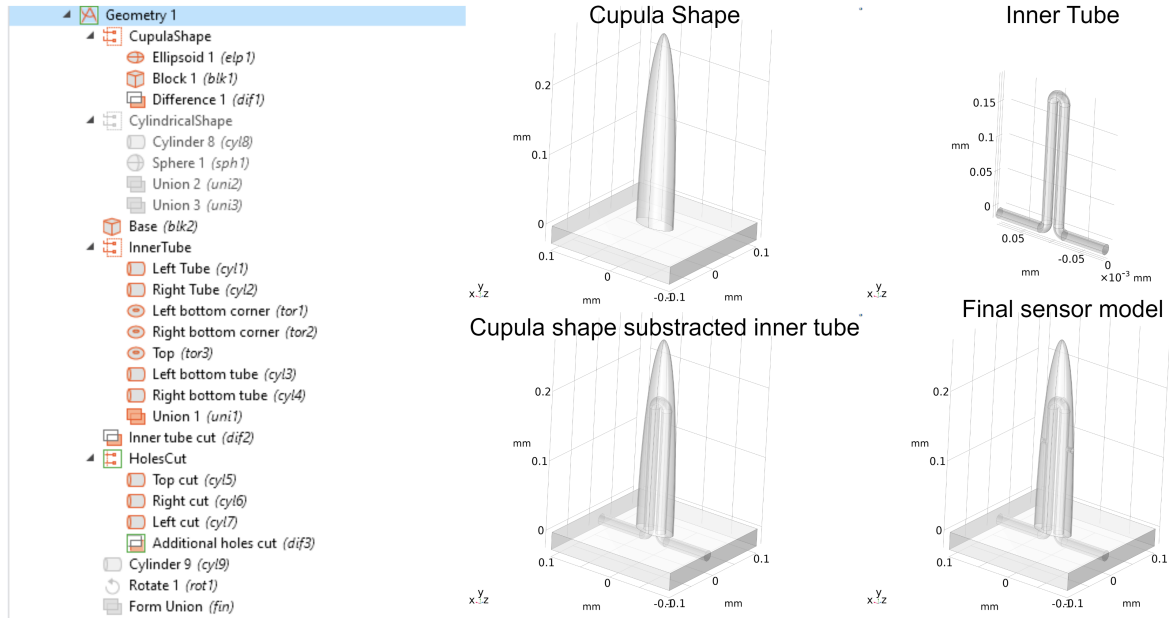
Fig. 4: This figure contains 1:2 ellipsoid sensor. The left image shows the geometry building tree. The operations are arranged into 3 main groups: "Cupula shape", "Inner tube", and "Holes cut". The cylindrical shape group is suppressed unless a cylindrical sensor model is built. On the right, there are 4 pictures depicting the building steps of a sensor 3D model

as an outlet. In this configuration, the liquid became stuck at the top of the sensor, where the tube makes a sharp turn. Additional canals help mitigate this issue by creating a new outlet at the points where the liquid used to be stuck. Canals have a radius of $0.00375[mm]$, half of the inner tube radius. One is positioned at the top of the inner tube, where the air pocket could form, and two at the side to help the flow of the liquid.

The last thing to mention about the sensor model is its orientation inside the software. In figure 4 the x, y, and z-axis orientation can be found in the bottom left corner of each 3D model picture. Inside the simulation the flow at an angle 0 $[deg]$ will point in the direction of the z-axis. Later in this report, the different directions will be simply called x-, y-, and z-direction.
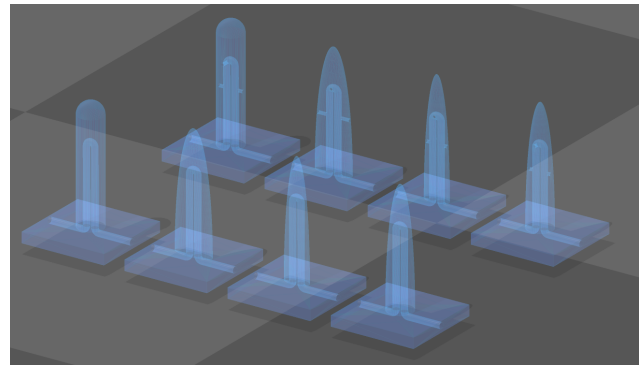

Fig. 5: The figure shows finished 3D models of all sensors. Models in the upper row have additional canals cut out. From left to right the sensors are: cylindrical, ellipsoid 1:3, 1:2, and 1:1.

B. Variables

There are several variables added to the simulation file. First, the sensor body height, width, and thickness are defined. In the previous section, all the dimensions were given

explicitly, but in the simulation file all the parameters that are dependent on the sensor dimensions, such as geometry size and position, are defined through the aforementioned variables to make the simulation modification-friendly. Other important variables are inlet fluid velocity $u\_in[m/s]$ and flow orientation $O[deg]$. Those variables are used during the simulation to iterate through several flow velocities and orientations.

C. Simulation settings

The simulation setup begins by choosing all the required physics modules. For this simulation, solid mechanics and fluid-structure interaction physics are required. The software automatically adds the laminar flow module. Next, the 3D model, described in the previous section, is built using the COMSOL geometry tools. Additionally, the sensor is positioned inside a $4[mm]$ in height and $1[mm]$ in radius cylinder, which is used to define water flow boundaries. The cylinder is also rotated around the y-axis by an angle of O to set the flow orientation. Materials are assigned to each geometry entity. The sensor body is made out of PDMS, which is one of the built-in materials. It is located under the material tab in the MEMS/Polymers folder. The cylinder material is assigned to water and is added to deforming domain node under the moving mesh folder. The sensor geometry is assigned to solid mechanics physics. The cylinder is assigned to laminar flow physics. The surface boundaries of the cupula deform based on both flow around it and the mechanical deformation of the cupula body and are added under the fluid-structure interaction node.

After all the geometry is assigned to the correct physics, the system constraints are added. One of the bases of the cylinder is defined as an inlet with fully developed flow and fluid average velocity set to u_in. The other base is defined as an outlet. The lateral surface of the cylinder is defined as a wall. The bottom face of a cuboid sensor base is fixed in space to prevent the sensor from flowing out of the tube.

D. Test setup

Two stationary studies are used for conducting tests. One is for a change in flow velocity u_in and another for a change in flow orientation O. Initially, the parametric sweep was used to iterate through all u_in and O values. In the first round of simulations velocities from 0.1 to $1[m/s]$, with the step of 0.1, and 7 angles from 0 to $90[deg]$, with the step of 15, were tested. Due to the presence of planes of symmetry in the sensor bodies in the xy and zy planes, the angle study data, covering angles from 0 to 90 degrees, can be extrapolated to encompass a full rotation. The angle is fixed to $0[deg]$ during the velocity study and the velocity is set to $1[m/s]$ during the angle study. The first issue occurred at the angle of 60 deg when the simulation for the ellipsoid 1:2 sensor failed to compute. The reason for this is still unclear and the angle was changed to 61 for all other shapes and subsequent studies. Another issue occurred at an angle of 90 deg. Ellipsoids 1:2 and 1:3 resist bending in the x-direction more than in the z-direction due to their geometry. When the flow is exactly at 90 deg, there exist two possible solutions where the sensor is inclined more to the left or the right. This effect can

be clearly seen in the appendix XII-H, where the ellipsoid 1:3 sensor does not bend in the direction of the flow when the flow is at 89 [*deg*]. To avoid this uncertainty, the angle was changed to 89 deg for subsequent simulations. In the second round of simulations, it was decided to simulate higher flow velocities values to investigate when the sensor tip displacement saturates. Also, a smaller angle step was chosen to get a better plot resolution. Velocities from 0.1 to 1.7[*m/s*], with the step of 0.1, and angles of 10, 20, 30, 40, 50, 61, 70, 80, and 89 [*deg*] were tested. The angle study was a success, while flow velocities higher than 1 [*m/s*] caused a failure in the simulation. COMSOL did not specify the failure reasons. The first proposed solution was to increase the mesh density. While this partially solved the problem, higher flow velocity values still failed to compute and the computational time became prohibitively large. After studying official COMSOL guides (COMSOL 2023a), a solution was found. The parametric sweep was changed to an auxiliary sweep. The prime differences between the two are that the parametric sweep can handle the geometry change between simulation runs but will start the simulation from the initial geometry position for each change in a variable while the auxiliary sweep only works when geometry remains the same but can use the previous solution as a starting point in a new simulation. This results in a faster simulation and successful computation for higher fluid velocities.

The reason for the simulations to be run only up to a fluid velocity of 1.7 [*m/s*] is that the simulation becomes less stable as velocity increase, with some sensor models failing to compute for higher velocities. Figure 6 show a convergence plot for a cylindrical sensor velocity study from the final simulation run. As the velocity increases, the stability of the model convergence gradually diminishes. Due to the time constraints of this project the velocity of 1.7 [*m/s*] turned out to be the maximum value for which all models were successfully tested.
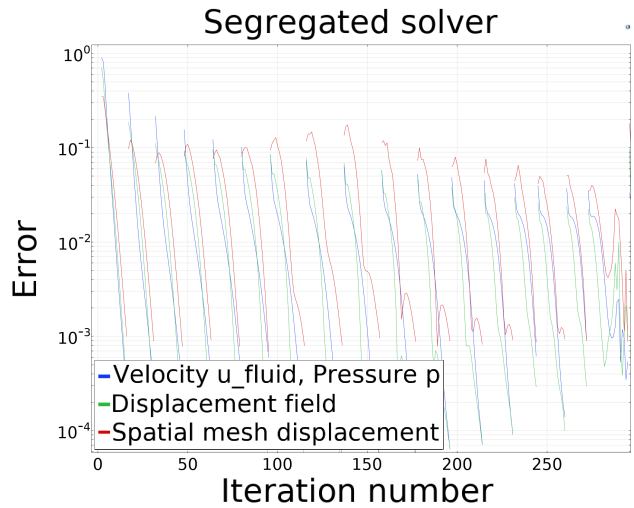

Fig. 6: A convergence plot for a cylindrical sensor velocity study. Each set of lines represents an increase in velocity by 0.1 [*m/s*]. After the solution error becomes small enough, the simulation begins a new run with updated fluid velocity, using the previous solution as a starting point. The final set of lines shows the convergence plot for the velocity of 1.7 [*m/s*]

E. Mesh optimization

COMSOL uses finite element analysis for the simulations (COMSOL 2017) and requires a geometry mesh for simulated models. Several mesh densities were tested to find a balance between simulation speed and accuracy. A denser mesh offers a more accurate representation of sensor geometry, resulting in a simulation that is a better approximation of real-world sensor

behavior. However, increase in accuracy comes at the cost of longer computation times. Five mesh densities were tested ranging from normal to extremely coarse. Figure 7 shows the tip displacement of an ellipsoid 1:2 sensor for all mesh densities. As can be seen, all the meshes lead to the same displacement curve with an extremely coarse mesh having the highest deviation. The coarser mesh was chosen for all the simulations because it is close enough to the normal density mesh while taking only a third of the time to compute.
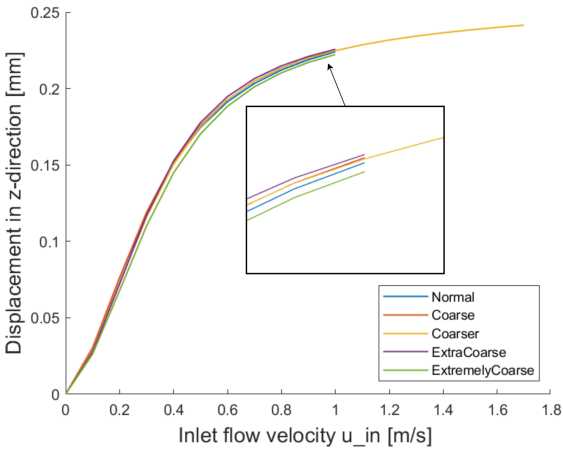

Fig. 7: Tip displacement of an ellipsoid 1:2 sensor for five mesh densities: normal, coarse, coarser, extra coarse, and extremely coarse.

F. Segregated versus Fully coupled approach

FSI simulation requires the use of multiple physics modules. As a result, the researcher is faced with the choice of conducting either a segregated or fully coupled simulation. A fully coupled approach forms a single system of equations that incorporates all the physics involved and solves it. A segregated approach creates a separate system of equations for each physics and another system of equations specif-

ically for areas that are directly affected by multiple physics. In the case of the sensor model the sensor body is affected by solid mechanics, the cylinder water pipe is affected by laminar flow physics and only the outer shell of the sensor body is directly affected by both. As stated by the official COMSOL guide (COMSOL 2023b), the fully coupled approach is often more robust and converges using fewer iterations, but has a larger memory requirement and takes a longer time. Figure 8 shows tip displacement versus fluid velocity test results for the ellipsoid 1:2 sensor using both approaches. As can be seen, there is no measurable difference between the two techniques. A segregated approach is used for all other tests because it requires less time and computer memory.
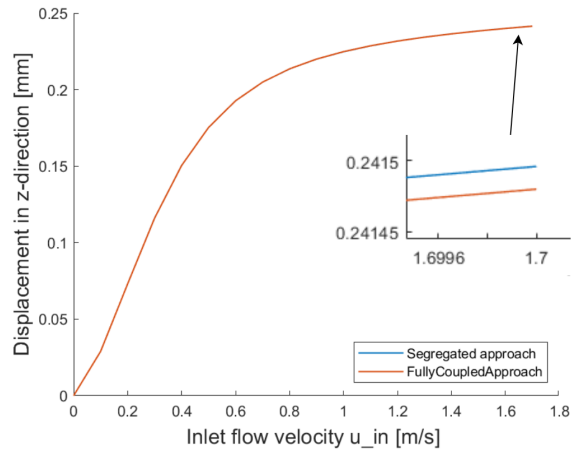

Fig. 8: Tip displacement of an ellipsoid 1:2 sensor using segregated and fully coupled approaches.

VI. RESULTS

After the simulation is conducted the results are stored as a solution file inside COMSOL. There are 4 main parameters of interest: tip

displacement, stress at the base, stress inside the inner tube, and the inner tube elongation.

A. Tip displacement

A 1D plot group with a point graph is created to display the tip displacement. Figure 9 contains the tip displacement of different cupula shapes under various fluid flow velocities, where the x-axis shows inlet flow velocity $u\_in[m/s]$ and the y-axis show tip displacement in the direction of the flow. Initially, only study up to 1 m/s inlet flow velocity were conducted. As evident from the graph, at this velocity the displacement of cylindrical and 1:1 ellipsoid sensors is not saturated, so higher velocities were also tested in the final studies. Figure 10 contains the tip displacement in the z-direction against various fluid flow angles. The sinusoidal function with a period of 360 $[deg]$ is added to each plot to be used as a reference in the discussion section.
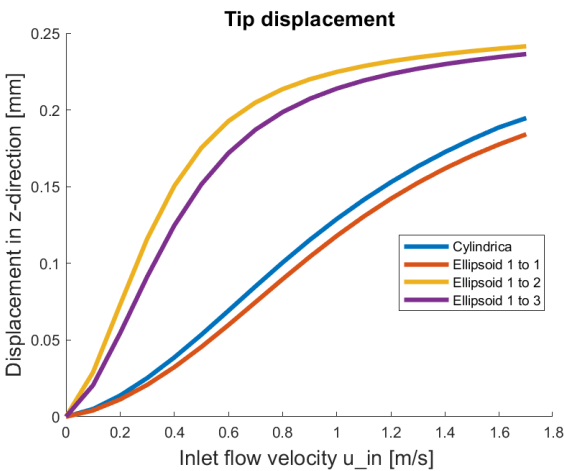

Fig. 9: Tip displacement of four cupula shapes in the z-direction for velocities from 0 to 1.7 $[m/s]$
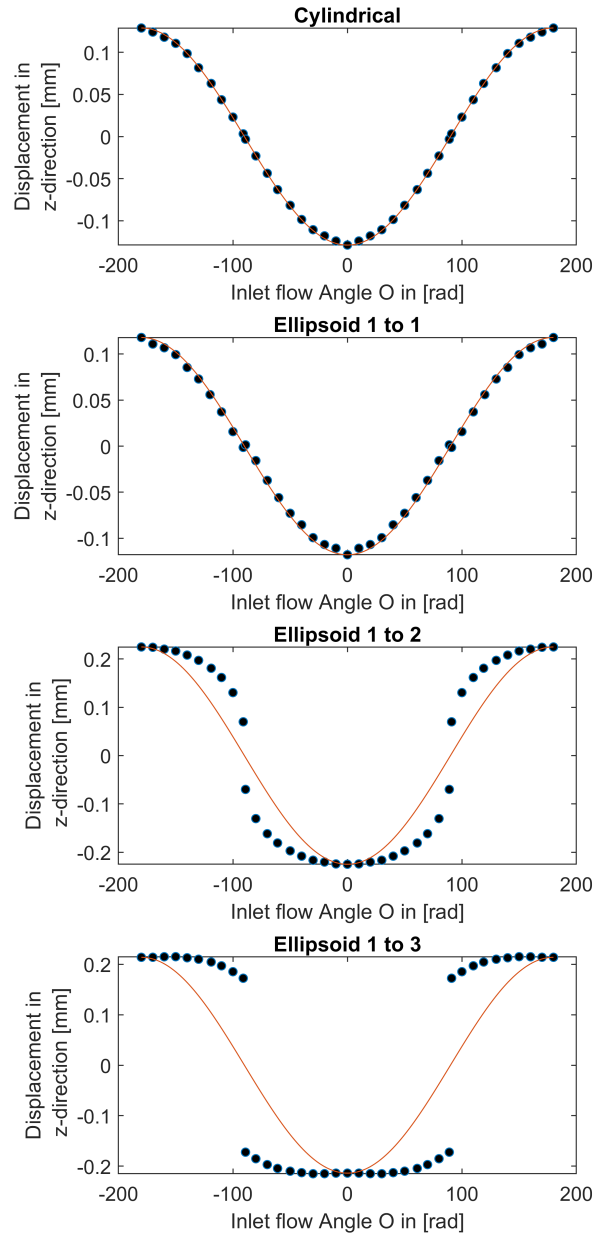

Fig. 10: Tip displacement of four cupula shapes in the z-axis direction for angles from -180 to +180 $[deg]$. The flow velocity is set to 1 $[m/s]$
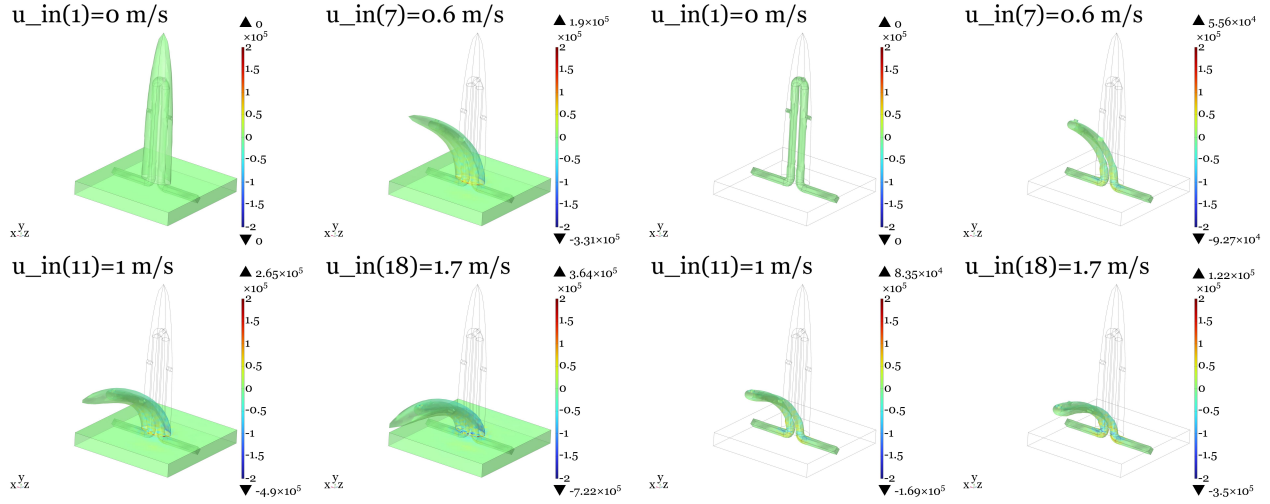
14

Fig. 11: Stress plot of the cupula and inner tube for flow velocities of 0.0, 0.6, 1.0, and 1.7 [*m/s*].
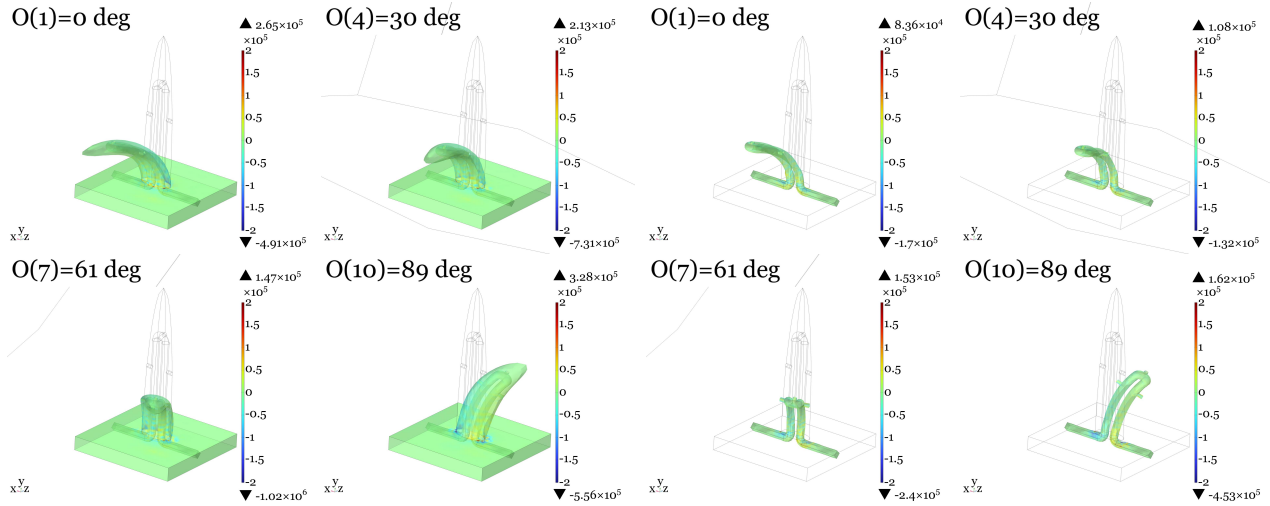
Fig. 12: Stress plot of the cupula and inner tube for flow angles of 0, 30, 61, and 89 [*deg*].

B. Stress

A 3D plot group is created to display the stress experienced by the sensor during deformation. A volume plot is used for displaying the stress at the base. Figures 12 and 11 show the plots for the ellipsoid 1:2 sensor. Plots for the other shapes can be found in the appendix. The plot colors the model based on the stress it experiences at a particular point. All the plots have the color range fixed from −200 to +200 [*KPa*] to make it easier to compare stress plots of different sensor shapes. The maximum and minimum stress experienced by the sensor can be found above or below the color legend. The stress used for the plots is the pressure, instead of commonly used von Mises or Tresca stresses because it is important to see whether the part experience stress or strain at a particular point. Another 3D plot group with the surface plot is created to display stress on the surface of the

15

inner tube. Only the surface of the inner tube is added to the plot, while other parts of the sensor are hidden. Figure 12 shows the same two plots for the change in flow angle.
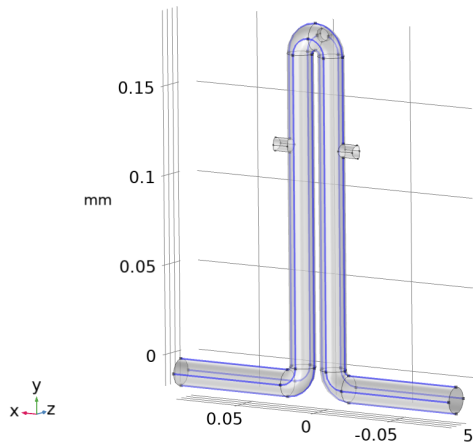
C. Inner tube deformation

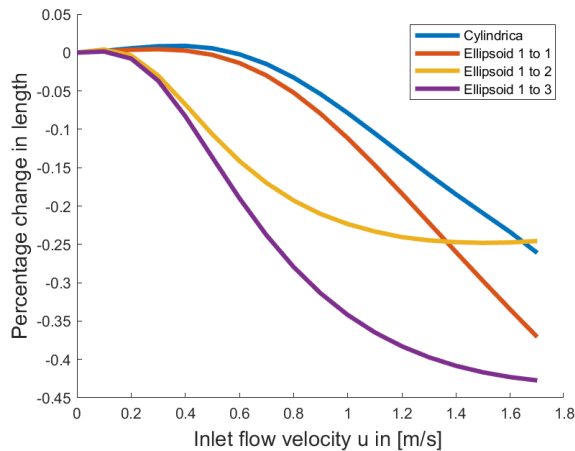Fig. 13: Sensor inner tube. Four outer lines are highlighted

Fig. 14: Inner tube length percentage change for flow velocities from 0 to 1.7 $[m/s]$

The inner tube central line deformation is an important parameter because it directly influences the real-world sensor output. Unfortunately, this information cannot be extracted from COMSOL because the inner tube is modeled as an empty canal inside the sensor. As can be seen from figure 13, there are four lines running along the outer shell of an inner tube. One of the ways to measure the length of each line inside COMSOL is to integrate the number 1 along the line length. Each line length is measured for all fluid velocities and angles. Next, a percentage change is calculated for each line using the equation 1. The average of 4 line length percentage change is taken to approximate the inner line length percentage change. One could ask why specifically this procedure is used to approximate the central line length change instead of, for example, averaging the final length of all four lines. When a shape is deformed by stretching or compressing, the lengths of the individual lines on its surface change. However, these changes in length may not be uniform across the entire shape. Some parts of the shape may experience more stretching or compression than others, resulting in a non-uniform deformation. If one were to simply calculate the average of the lengths of the four outer lines without considering the scaling factor, it would require the assumption that the deformation is uniform and equal across all parts of the shape. There is no reason to believe this assumption is true in the case of the sensor's inner tube. By calculating the scaling factor for each outer line and then finding the average of these scaling factors, one considers the variations in deformation across different parts of the shape. This average scaling factor provides a better estimation of the overall deformation that occurred along the shape's path. The percentage change in inner

16

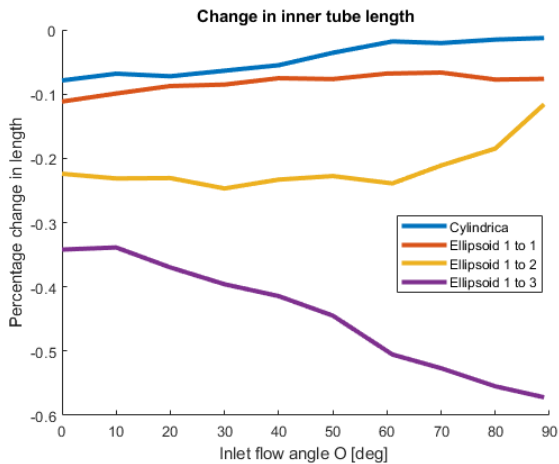$$Outer\ line\ length\ percentage\ change = (\frac{Final\ length}{Initial\ length} - 1)/100 \qquad (1)$$

Fig. 15: Inner tube length percentage change for flow angles from 0 to 89 $[m/s]$

tube length is shown in figure 14 for different flow velocities and figure 15 for different flow angles.

VII. Discussion

The following section contains an analysis of all the results shown in the previous section.

A. Tip displacement versus velocity

As can be seen from figure 9 the lines can be separated into two groups. The first group consists of ellipsoid 1:2 and 1:3 sensors. The second group consists of cylindrical and ellipsoid 1:1 sensors. The main difference between sensors from each group is the sensor thickness. Sensors from group one have a thickness of 0.015 $[mm]$ while sensors from group two are 0.03 $[mm]$ thick. The first group's tip displacement increases faster as the flow velocity increase when compared to the second group. The first group tip displacement also saturates

earlier and at a higher value of 0.24 $[mm]$. The second group's tip displacement does not reach saturation within the range of tested flow velocities. Another interesting behavior is that the ellipsoid 1:3 sensor deforms less than the ellipsoid 1:2 sensor even though it is wider and experience a higher force from the fluid flow around it. One explanation is that increased structural rigidity, provided by additional material, outweighs increased force from fluid flow. Nevertheless, both ellipsoid 1:2 and 1:3 sensors have almost the same maximum tip displacement.

Based on the tip displacement graph it could be said that the first sensor group is more sensitive to the flow velocity changes and will work for slower water flows with the ideal water flow velocity range being 0.1 to 0.6 $[m/s]$. On the other hand, the second group is less sensitive but is suitable for higher fluid flow velocities, however, it is unclear at what fluid velocity the change in tip displacement becomes too little to accurately measure.

B. Tip displacement versus angle

In theory, a tip displacement versus angle graph of a cylinder positioned in a laminar flow will follow a sinusoidal curve. Any deviation from the sinusoidal curve implies some degree of directionality in the sensor behavior. As can be seen from figure 10 cylindrical and ellipsoid 1:1 sensors closely follow the sinusoidal curve, while ellipsoid 1:2 and 1:3 sensors deviate significantly. As was mentioned in section V-

D, due to the difference in thickness and width it is easier for the ellipsoid 1:2 and 1:3 sensors to bend in the direction of their minor axis rather than their major axis. This behavior is especially apparent in the ellipsoid 1:3 plot. The tip makes a large jump as soon as the flow angle increase above 90 [deg], at which point the sensor tip falls to the other side. On the other hand, as the flow angle changes, cylindrical and ellipsoid 1:1 sensors' tip displacement gradually changes, because their bending direction is always aligned with the flow, as can be seen in appendix XII-B and XII-D.

C. Stress

The first and main conclusion from the stress plots is that the stress is concentrated where the cupula is attached to the cuboid base. Furthermore, the inner tube is experiencing stress not only near the cupula stress concentration but also inside the cuboid base where the tube makes a turn, as can be seen in figure 16.
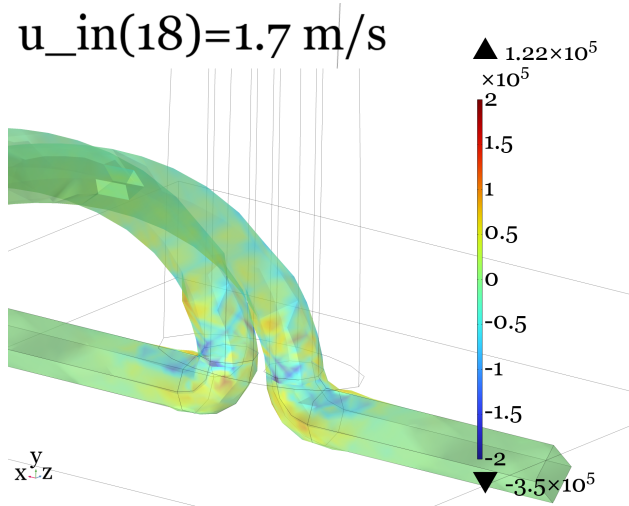

Fig. 16: Stress inside the inner tube of ellipsoid 1:2 at flow velocity of 1.7 [m/s] and flow angle of 0 [deg]

For the highest fluid velocity of 1.7 [m/s]

the maximum stress is 650 [kPa] for cylindrical, 576 [kPa] for ellipsoid 1:1, 722 [kPa] for ellipsoid 1:2, and 1030 [kPa] for ellipsoid 1:3 sensors. According to the MIT material property database, PDMS has a fracture strength of 2560 [kPa] (MIT 2004), thus all the sensor will maintain their structural integrity when subjected to tested fluid velocities.

Another thing to note is the change in the distribution of tensile and compressive stresses as the fluid velocity increase. At first, all the sensors bend, creating an area of compressive stress on the inner side of the bend and tensile stress on the outer side of the bend. As the sensor body becomes more aligned with the fluid flow, the flow drag force starts pulling the sensor instead of bending it. This effect is best observed on the cylindrical sensor stress plot. As can be seen in figure 17 the base of the cylindrical sensor is experiencing predominantly tensile stress when the fluid velocity is at 1.7 [m/s].
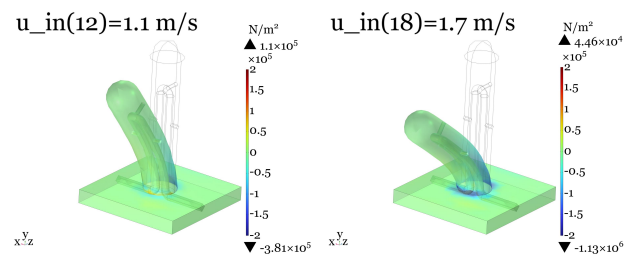

Fig. 17: Cylindrical sensor stress plot for flow velocities of 1.1 and 1.7 [m/s]

D. Inner tube deformation versus velocity

The first thing to notice from figure 14 is that the inner tube compresses when the sensor is subjected to the water flow. The compression seems to be inversely proportional to the tip

displacement up until the point where the sensor deformation is saturated. This is a desired result because the tube deformation is the only parameter that can be directly measured in a real sensor by measuring the resistance of the piezoresistive layer that covers the inner tube walls. These findings suggest that the sensor output can be successfully mapped onto the sensor tip displacement, although only for some velocity ranges. At higher flow velocities, the inner tube compression halts and even reverses for the ellipsoid 1:2 sensor. This is due to the phenomena explained in the previous section, where at higher velocities the water drag starts pulling the sensor instead of bending it, elongating the whole sensor body. Similar to tip displacement results, the ellipsoid 1:2 and 1:3 sensors are more suitable for lower flow velocities, while cylindrical and ellipsoid 1:1 sensors can be used at higher velocities. However, in contrast to the tip displacement graph, the inner tube length changes of ellipsoid 1:2 and 1:3 sensors exhibit significant deviations from each other, with the latter demonstrating an almost twofold decrease in percentage change in tube length when compared to the former at a maximum flow velocity. This means that ellipsoid 1:3 is a better candidate for sensor body shape.

E. Inner tube deformation versus angle

As can be seen in figure 15, as the flow angle approach 90 [*deg*], the sensors' inner tube deformation approach zero, with the exception of the ellipsoid 1:3 sensor. While ellipsoid 1:2 behavior can be explained by its directionality, another explanation is required for cylindrical and ellipsoid 1:1 sensors. One of the reasons for

this behavior could be the inner tube geometry. As was shown in the section V-A, the inner tube consists of two vertical cylinders that merge near the sensor tip. When the flow angle is 0 [*deg*], both cylinders bend in the same way. However, when the flow angle is near 90 [*deg*], the cylinder further along the flow mostly compresses, while the other cylinder mostly elongates. When the deformation is averaged, elongation and compression cancel each other out, resulting in the same tube length as when the sensor is at rest. This is not the case for the ellipsoid 1:3 sensor. Due to the high degree of directionality, the sensor is never displaced enough for one of the cylinders to become elongated. On the opposite, the sensor is further compressed, decreasing the final inner tube length.

F. Summary

The simulation results showed that the ellipsoid 1:2 and 1:3 sensors exhibited higher tip displacement compared to the cylindrical and ellipsoid 1:1 sensors. This suggests that the ellipsoid 1:2 and 1:3 sensors have higher strain and have a better chance of producing measurable output. Furthermore, the ellipsoid 1:2 and 1:3 sensors had a faster increase in tip displacement, meaning they are more sensitive to flow velocity change.

The stress analysis results indicated that all sensors maintained their structural integrity within the tested fluid velocities, with the highest stress experienced at the attachment point of the sensor body to the cuboid base. Among all sensors, an ellipsoid 1:3 sensor had the highest maximum stress.

A higher change in inner tube length indicates higher strain experienced by the piezoresistive material. The simulation results showed that the ellipsoid 1:3 sensor had the highest inner tube compression for the tested fluid velocities. This implies that the ellipsoid 1:3 sensor may experience higher strain and deformation, making it a favorable body shape choice

Based on this summary, it can be proposed that the ellipsoid 1:3 sensor is the best-performing shape considering the sensor performance criteria outlined in section IV-D. It exhibits the highest stress and inner tube deformation while having the second-highest tip displacement, making it a promising candidate for further investigation.

VIII. CONCLUSION

At the end of the problem context section of this report, a central research question and three sub-questions were stated. The findings obtained while working with COMSOL software provide answers to all proposed questions. The following paragraphs will answer each question one by one.

A. What is the right procedure for creating a sensor 3D model?

Section V-A goes over the process of creating a sensor model. It contains all the necessary information for recreating the same sensors investigated in this project. All the dimensions follow the supervisor's requirements, hence the final model is an accurate representation of the real-world sensor.

B. What are the simulation settings for the required tests?

Sections V-B through V-F go over all the required simulation setups. Solid mechanics, laminar flow, and fluid-structure interaction physics were all added to the simulation and correctly configured to successfully test sensor deformation when positioned inside the pipe with different flow velocities and orientations. Based on the mesh optimization study a coarser mesh was chosen as it offered the best computation time while following closely the results obtained using the finer mesh settings. Finally, a segregated approach was used when solving the simulation as it yielded the same results as a more accurate, fully coupled, approach while being considerably faster.

C. What is the structural behavior of the sensor under various flow conditions?

This project tested angles from 0 to 89 $[deg]$ and flow velocities up to 1.7 $[m/s]$. The data on flow orientation were extrapolated to fill a full circle of rotation and the step size was enough to see the overall shape of the graph. The tested flow velocities cover the working range of ellipsoid 1:2 and 1:3 sensors. However, the Cylindrical and ellipsoid 1:1 sensors did not reach saturation in tip displacement at the highest tested velocity. Testing faster flows could be the aim of future research. All the required metrics (stress, tip displacement, inner tube elongation) were successfully extracted from simulation data and presented in this report, thus answering this research question.

20

D. How does the shape of the sensor body affect the sensor performance under various fluid flow conditions?

All the results obtained were discussed in light of the performance criteria described in section IV-D. The first finding is that the thinner sensor is more flexible and reaches a higher tip displacement for the same fluid velocity compared to thicker sensors. The thinner sensor also reaches tip displacement saturation earlier and will not work for faster flows. Increasing the width of the sensor does not increase the tip displacement, however, the sensor develops higher stress and inner tube deformation. A wider sensor also becomes more directional and resists bending in the direction of the major axis. The ellipsoid 1:3 sensor showed the best performance among all tested shapes because the higher tip displacement, stress, and inner tube deformation are desirable.

IX. LIMITATIONS

The next paragraphs present some of the key limitations of the study that should be addressed in future research.

The first limitation of this project is that it was purely a simulation study, which may not fully capture the real-world complexities and variations in fluid flow. Experimental validation is necessary to confirm the findings and account for any discrepancies between the simulation and actual sensor behavior.

Another limitation is uncertainty about how accurately the tested metrics represent actual sensor performance. Other studies about artificial sensors are looking at what minimum and maximum deformation can be registered by measuring the sensor output voltage (Wissman et al. 2019) (McConney et al. 2009) (Kottapalli, Bora, et al. 2016) (Peleshanko et al. 2007), which is heavily dependent on the sensing mechanism and sensor production. Such investigation was not available for this project because the physics of the sensing mechanism isn't part of the simulated model and the sensor was not available for real-world testing.

The final limitation is that the research did not investigate the high enough flow velocities to see the full dynamics of cylindrical and ellipsoid 1:1 sensors. It is unclear what is the maximum tip displacement that can be reached by the thicker sensors and whether or not they develop higher stress and inner tube deformation than the ellipsoid 1:3 sensor.

X. FUTURE RESEARCH

Future research should address the limitations presented in the previous section. Real-world experiments should be performed to validate the simulation model's accuracy. The physical prototype will allow researchers to establish a relationship between the sensor output and the metrics measured in this project.

Also, higher flow velocities should be investigated to determine the behavior of thicker sensor shapes. An interesting study to consider is running a parametric sweep on a range of thicknesses and widths to find an optimal trade-off between tip displacement and sensor working range.

XI. REFERENCES

Bernoulli Institute for Mathematics, Computer Science and Artificial Intelligence (Mar. 2021). *Swarm collaborative multi-agent cyber physical systems with shared sensing modalities, 5G communication and micro-electromechanical sensor arrays (SMART-agents)*. URL: `https : / / www . nwo . nl / en / projects/18024`.

Bora, Meghali et al. (Jan. 2018). "Sensing the flow beneath the fins". In: *Bioinspiration &amp Biomimetics* 13.2, p. 025002. URL: `https://doi.org/10. 1088/1748-3190/aaa1c2`.

COMSOL (2017). *Detailed Explanation of the Finite Element Method (FEM) comsol.com*. `https : / / www.comsol.com/multiphysics/finite- element-method`. [Accessed 10-May-2023].

– (2023a). *Improving convergence of nonlinear stationary models*. URL: `https : / / www . comsol . com/support/learning-center/article/ Improving-Convergence-of-Nonlinear- Stationary-Models-66431`.

– (2023b). *Understanding the fully coupled vs. segregated approach and direct vs. iterative linear solvers*. URL: `https://www.comsol.com/support/ knowledgebase/1258`.

Kottapalli, Ajay Giri Prakash, Meghali Bora, et al. (Jan. 2016). "Nanofibril scaffold assisted MEMS artificial hydrogel neuromasts for enhanced sensitivity flow sensing". In: *Scientific Reports* 6.1. URL: `https: //doi.org/10.1038/srep19336`.

Kottapalli, Ajay Giri Prakash, Zhiyuan Shen, et al. (Jan. 2017). "Polymer MEMS sensor for flow monitoring in biomedical device applications". In: *2017 IEEE 30th International Conference on Micro Electro Mechanical Systems (MEMS)*. IEEE. URL: `https://doi. org/10.1109/memsys.2017.7863487`.

McConney, Michael E. et al. (Aug. 2009). "Bioinspired Material Approaches to Sensing". In: *Advanced Functional Materials* 19.16, pp. 2527–2544. URL: `https : / / doi . org / 10 . 1002 / adfm . 200900606`.

McHenry, Matthew J. and Sietse M. van Netten (Dec. 2007). "The flexural stiffness of superfi-

cial neuromasts in the zebrafish(Danio rerio) lateral line". In: *Journal of Experimental Biology* 210.23, pp. 4244–4253. eprint: `https : / / journals . biologists.com/jeb/article-pdf/210/ 23/4244/1261547/4244.pdf`. URL: `https: //doi.org/10.1242/jeb.009290`.

McHenry, Matthew J., James A. Strother, and Sietse M. van Netten (Aug. 2008). "Mechanical filtering by the boundary layer and fluid–structure interaction in the superficial neuromast of the fish lateral line system". In: *Journal of Comparative Physiology A* 194.9, pp. 795–810. URL: `https://doi.org/ 10.1007/s00359-008-0350-2`.

MIT (Feb. 2004). *Material: PDMS (polydimethylsiloxane)*. URL: `https://www.mit.edu/~6.777/ matprops/pdms.htm`.

Montgomery, John C., Shane Windsor, and Daniel Bassett (2009). "Behavior and physiology of mechanoreception: separating signal and noise". In: *Integrative Zoology* 4.1, pp. 3–12. eprint: `https : / / onlinelibrary.wiley.com/doi/pdf/10. 1111/j.1749-4877.2008.00130.x`. URL: `https://onlinelibrary.wiley.com/doi/ abs/10.1111/j.1749-4877.2008.00130. x`.

Netten, Sietse M. van (Nov. 2005). "Hydrodynamic detection by cupulae in a lateral line canal: functional relations between physics and physiology". In: *Biological Cybernetics* 94.1, pp. 67–85. URL: `https: //doi.org/10.1007/s00422-005-0032-x`.

Peleshanko, S. et al. (Oct. 2007). "Hydrogel-Encapsulated Microfabricated Haircells Mimicking Fish Cupula Neuromast". In: *Advanced Materials* 19.19, pp. 2903–2909. URL: `https://doi.org/ 10.1002/adma.200701141`.

Saeedi, Milad, Amir Shamloo, and Ariz Mohammadi (2019). "Fluid-Structure Interaction Simulation of Blood Flow and Cerebral Aneurysm: Effect of Partly Blocked Vessel". In: *Journal of Vascular Research* 56.6, pp. 296–307. URL: `https://doi.org/10. 1159/000503786`.

Shamloo, Amir, Milad Azimi Nejad, and Milad Saeedi (Oct. 2017). "Fluid–structure interaction simulation of

a cerebral aneurysm: Effects of endovascular coiling treatment and aneurysm wall thickening". In: *Journal of the Mechanical Behavior of Biomedical Materials* 74, pp. 72–83. URL: https://doi.org/10.1016/j.jmbbm.2017.05.020.

Wang, Qian et al. (July 2021). "Engineered Mechanosensors Inspired by Biological Mechanosensilla". In: *Advanced Materials Technologies* 6.11, p. 2100352. URL: https://doi.org/10.1002/admt.202100352.

Windsor, Shane and Matthew McHenry (Dec. 2009). "The influence of viscous hydrodynamics on the fish lateral-line system". In: *Integrative and comparative biology* 49, pp. 691–701.

Wissman, James P. et al. (June 2019). "Capacitive Bio-Inspired Flow Sensing Cupula". In: *Sensors* 19.11, p. 2639. URL: https://doi.org/10.3390/s19112639.

XII. APPENDIX

A. Cylindrical sensor stress versus flow velocity results

The following is a collage of volume and surface plots displaying the stress developed in the cylindrical sensor under all simulated flow velocities and flow orientation at 0 $[deg]$. The title above each plot shows the flow velocity. All the plots have the color range fixed from -200 to $+200$ $[KPa]$. Above and below the color legends the maximum tensile and compressive stresses are shown.
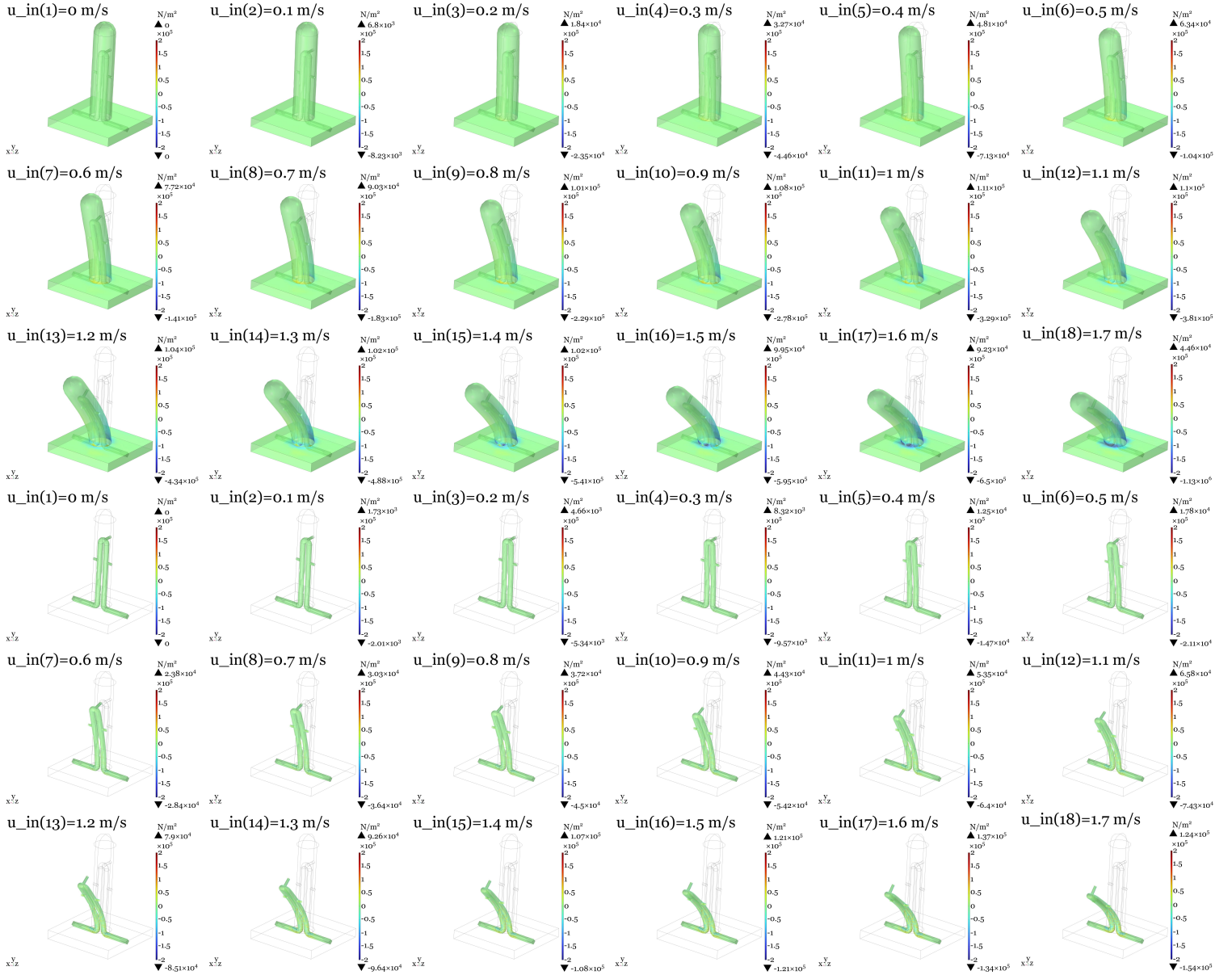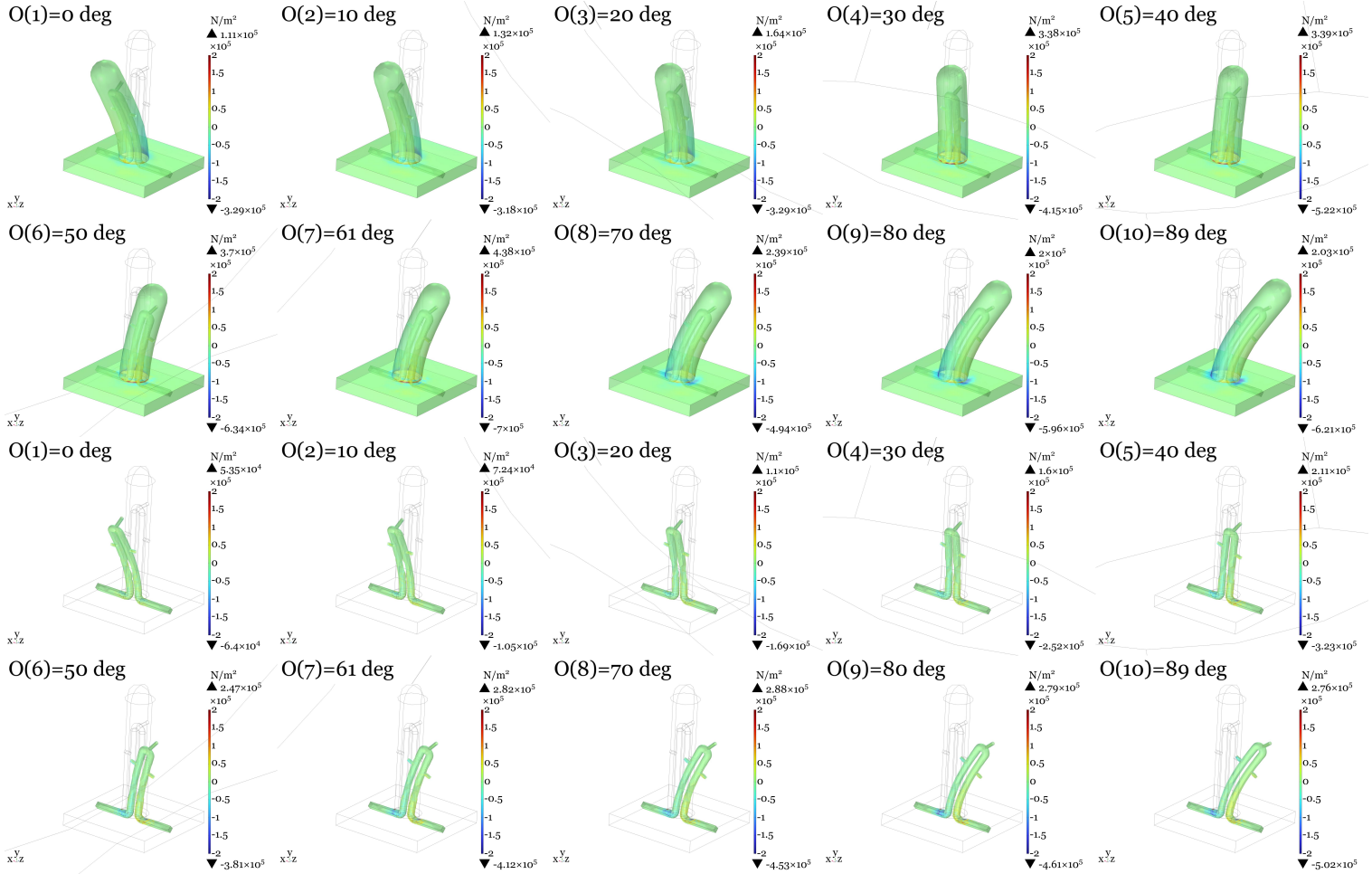

Fig. 18: Stress plot of the cupula and inner tube for all tested flow velocities.

B. Cylindrical sensor stress versus flow angle results

The following is a collage of volume and surface plots displaying the stress developed in the cylindrical sensor under all simulated flow orientations and at a flow velocity of 1 $[m/s]$. The title above each plot shows the flow angle. An angle of 0 $[deg]$ means the flow is oriented along the z-axis and an angle of 90 $[deg]$ means the flow is oriented along the x-axis. All the plots have the color range fixed from -200 to $+200$ $[KPa]$. Above and below the color legends the maximum tensile and compressive stresses are shown.
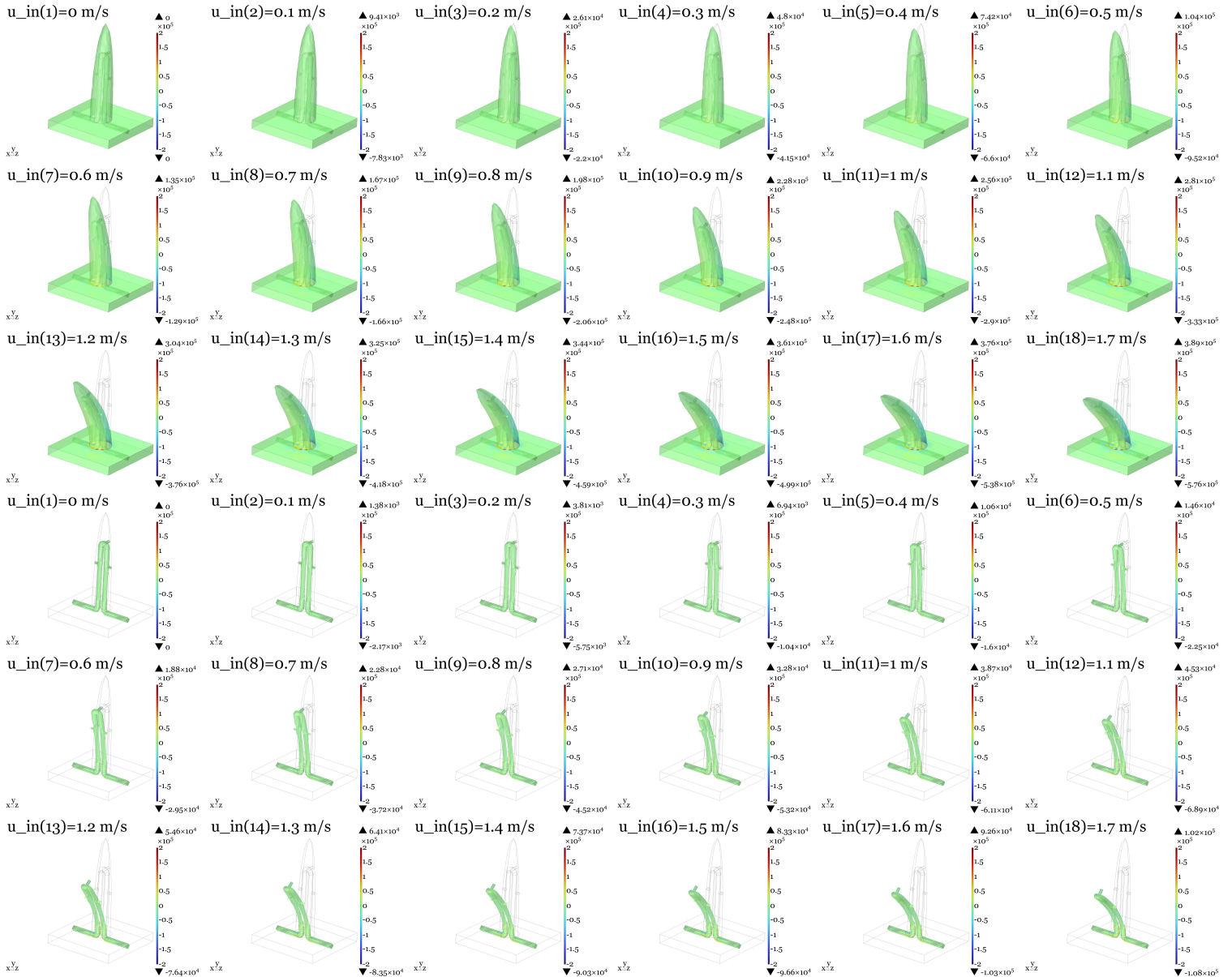

Fig. 19: Stress plot of the cupula and inner tube for all tested flow angles.

The following is a collage of volume and surface plots displaying the stress developed in the ellipsoid 1:1 sensor under all simulated flow velocities and flow orientation at 0 [*deg*]. The title above each plot shows the flow velocity. All the plots have the color range fixed from -200 to $+200$ [*KPa*]. Above and below the color legends the maximum tensile and compressive stresses are shown.

Fig. 20: Stress plot of the cupula and inner tube for all tested flow velocities.

26

D. Ellipsoid 1:1 sensor stress versus flow angle results

The following is a collage of volume and surface plots displaying the stress developed in the ellipsoid 1:1 sensor under all simulated flow orientations and at a flow velocity of 1 $[m/s]$. The title above each plot shows the flow angle. An angle of 0 $[deg]$ means the flow is oriented along the z-axis and an angle of 90 $[deg]$ means the flow is oriented along the x-axis. All the plots have the color range fixed from -200 to $+200$ $[KPa]$. Above and below the color legends the maximum tensile and compressive stresses are shown.
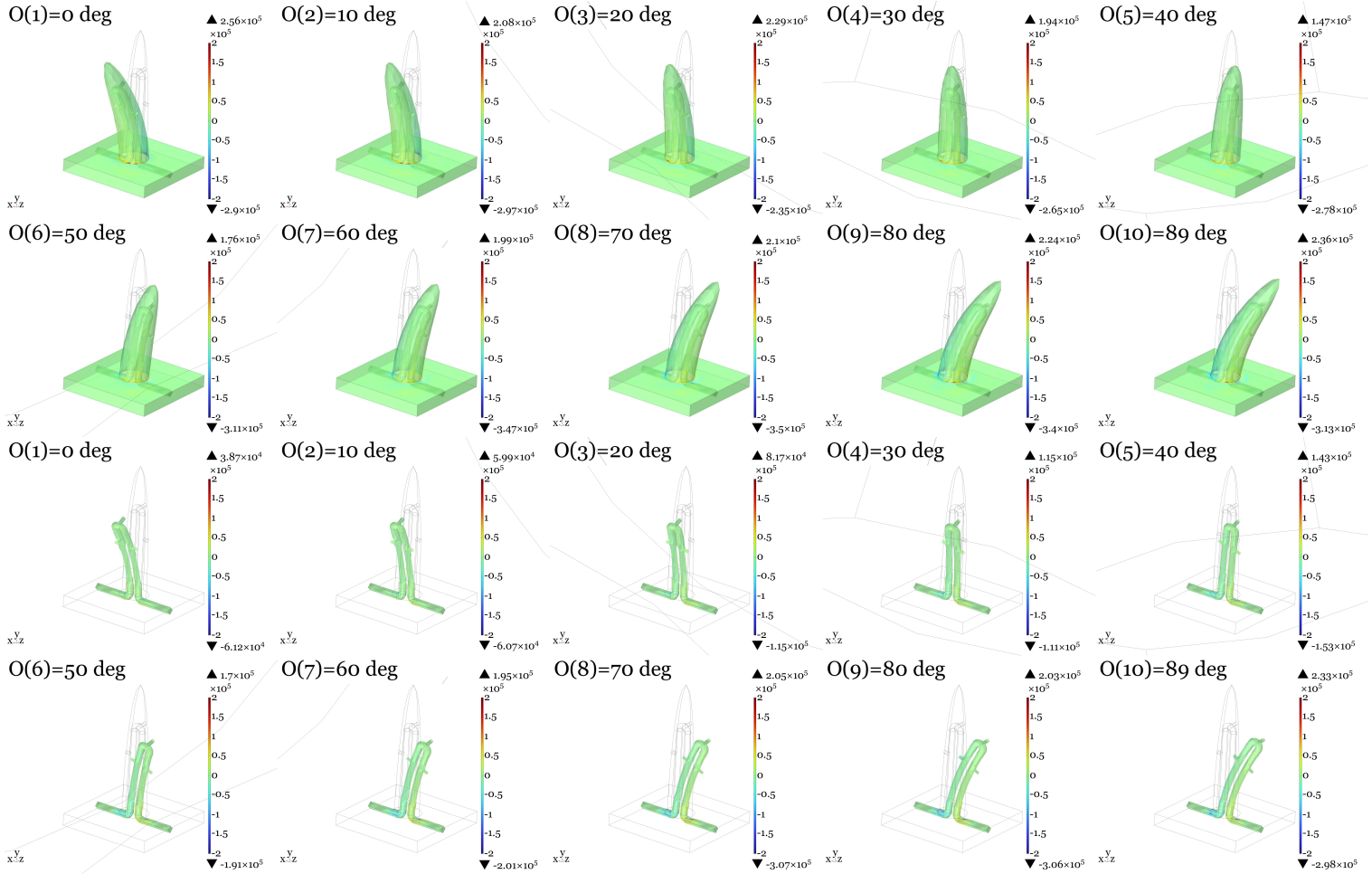

Fig. 21: Stress plot of the cupula and inner tube for all tested flow angles.

E. Ellipsoid 1:2 sensor stress versus flow velocities results

The following is a collage of volume and surface plots displaying the stress developed in the ellipsoid 1:2 sensor under all simulated flow velocities and flow orientation at 0 [*deg*]. The title above each plot shows the flow velocity. All the plots have the color range fixed from -200 to $+200$ [*KPa*]. Above and below the color legends the maximum tensile and compressive stresses are shown.
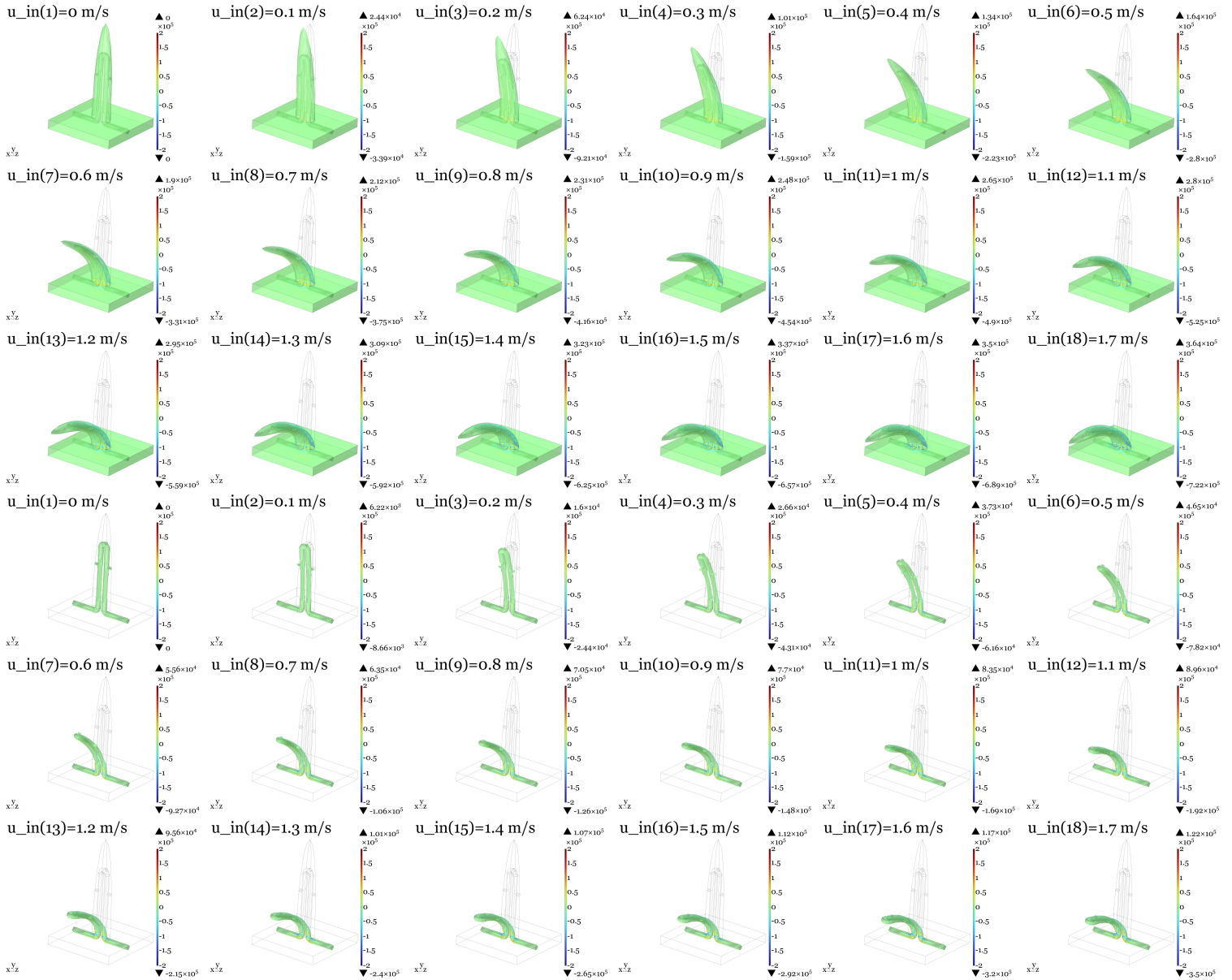

Fig. 22: Stress plot of the cupula and inner tube for all tested flow velocities.

28

F. Ellipsoid 1:2 sensor stress versus flow angle results

The following is a collage of volume and surface plots displaying the stress developed in the ellipsoid 1:2 sensor under all simulated flow orientations and at a flow velocity of 1 [m/s]. The title above each plot shows the flow angle. An angle of 0 [deg] means the flow is oriented along the z-axis and an angle of 90 [deg] means the flow is oriented along the x-axis. All the plots have the color range fixed from -200 to $+200$ [KPa]. Above and below the color legends the maximum tensile and compressive stresses are shown.
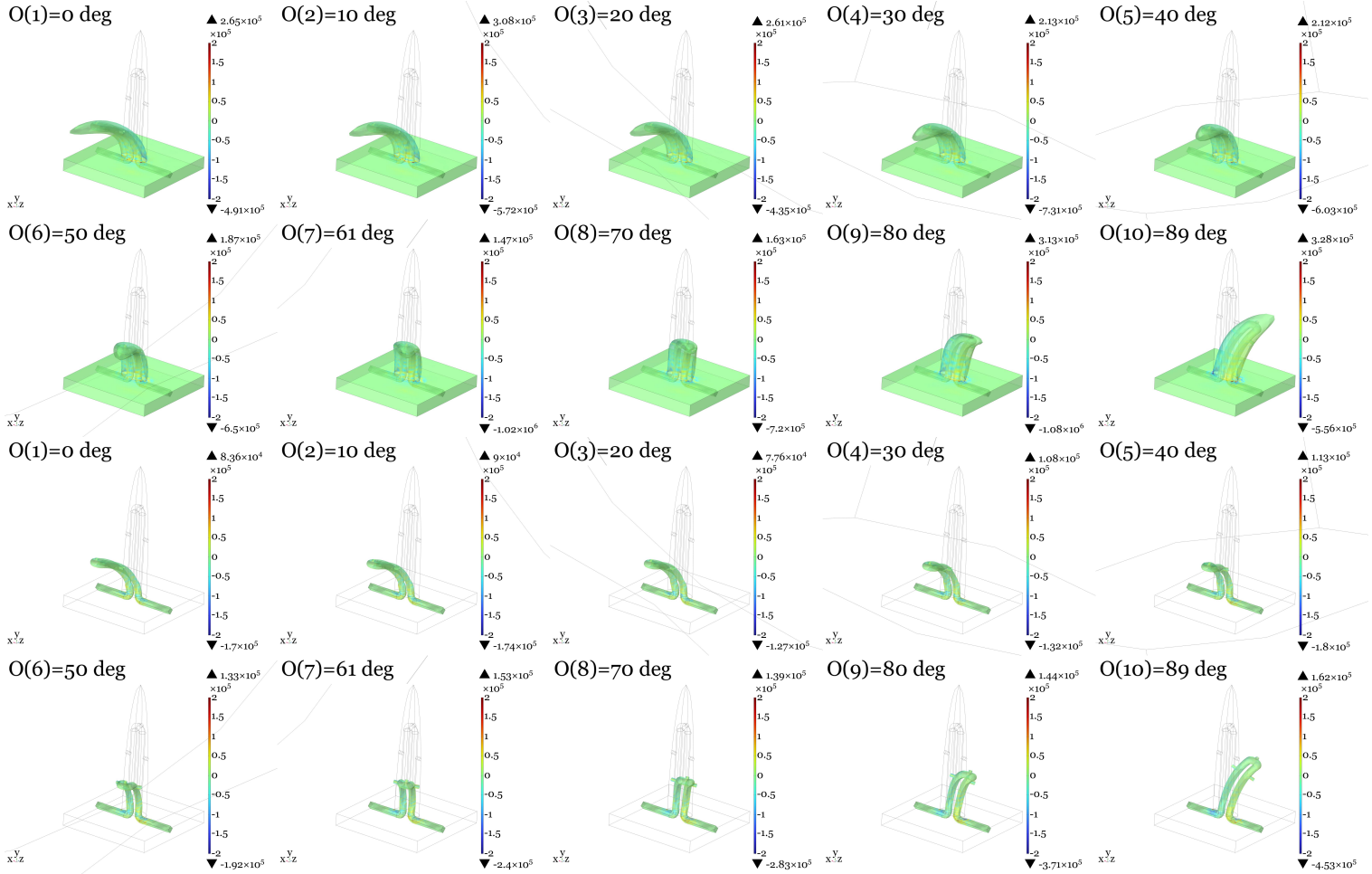

Fig. 23: Stress plot of the cupula and inner tube for all tested flow angles.

G. Ellipsoid 1:3 sensor stress versus flow velocities results

The following is a collage of volume and surface plots displaying the stress developed in the ellipsoid 1:3 sensor under all simulated flow velocities and flow orientation at 0 [*deg*]. The title above each plot shows the flow velocity. All the plots have the color range fixed from −200 to +200 [*KPa*]. Above and below the color legends the maximum tensile and compressive stresses are shown.
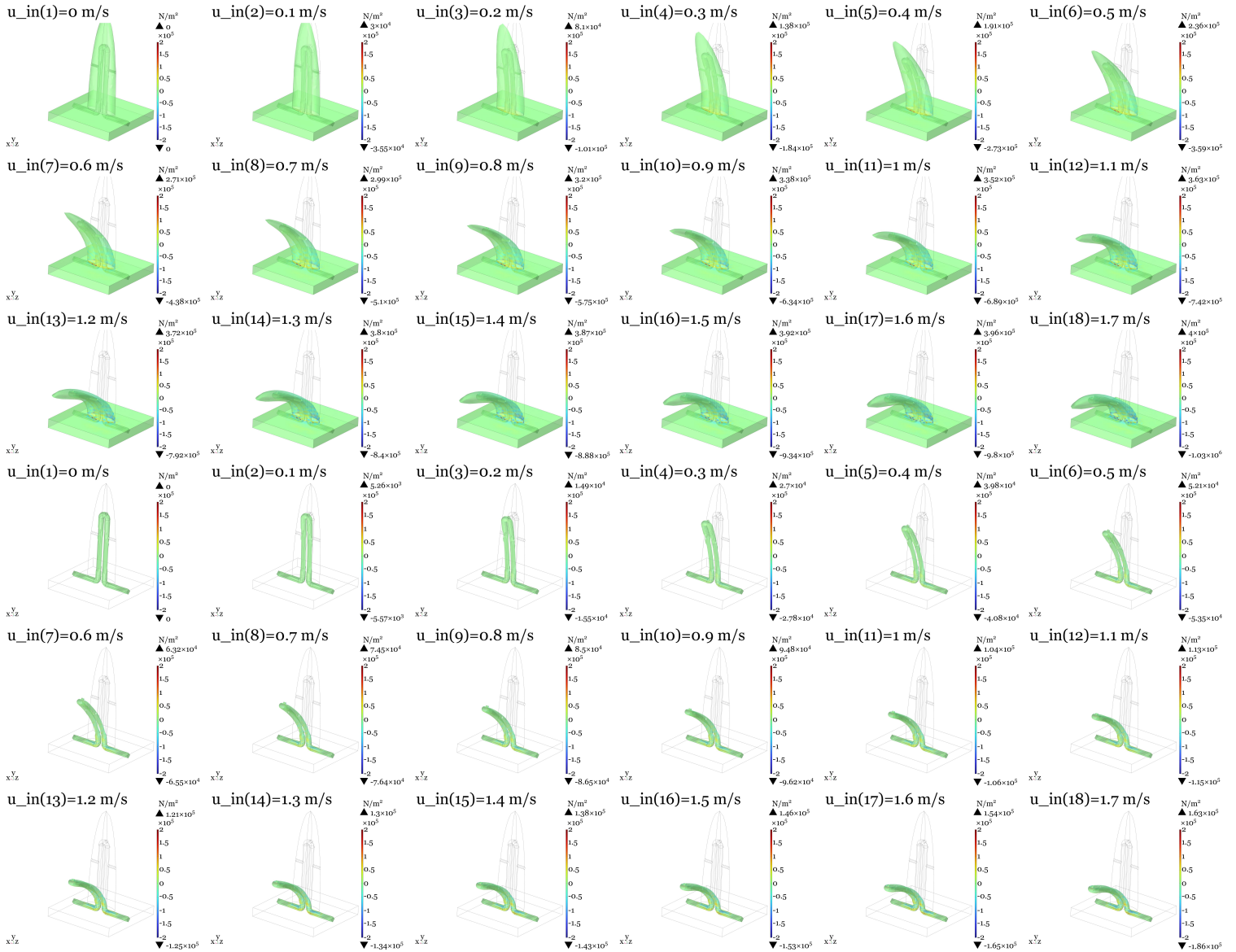

Fig. 24: Stress plot of the cupula and inner tube for all tested flow velocities.

H. Ellipsoid 1:3 sensor stress versus flow angle results

The following is a collage of volume and surface plots displaying the stress developed in the ellipsoid 1:3 sensor under all simulated flow orientations and at a flow velocity of 1 $[m/s]$. The title above each plot shows the flow angle. An angle of 0 $[deg]$ means the flow is oriented along the z-axis and an angle of 90 $[deg]$ means the flow is oriented along the x-axis. All the plots have the color range fixed from -200 to $+200$ $[KPa]$. Above and below the color legends the maximum tensile and compressive stresses are shown.
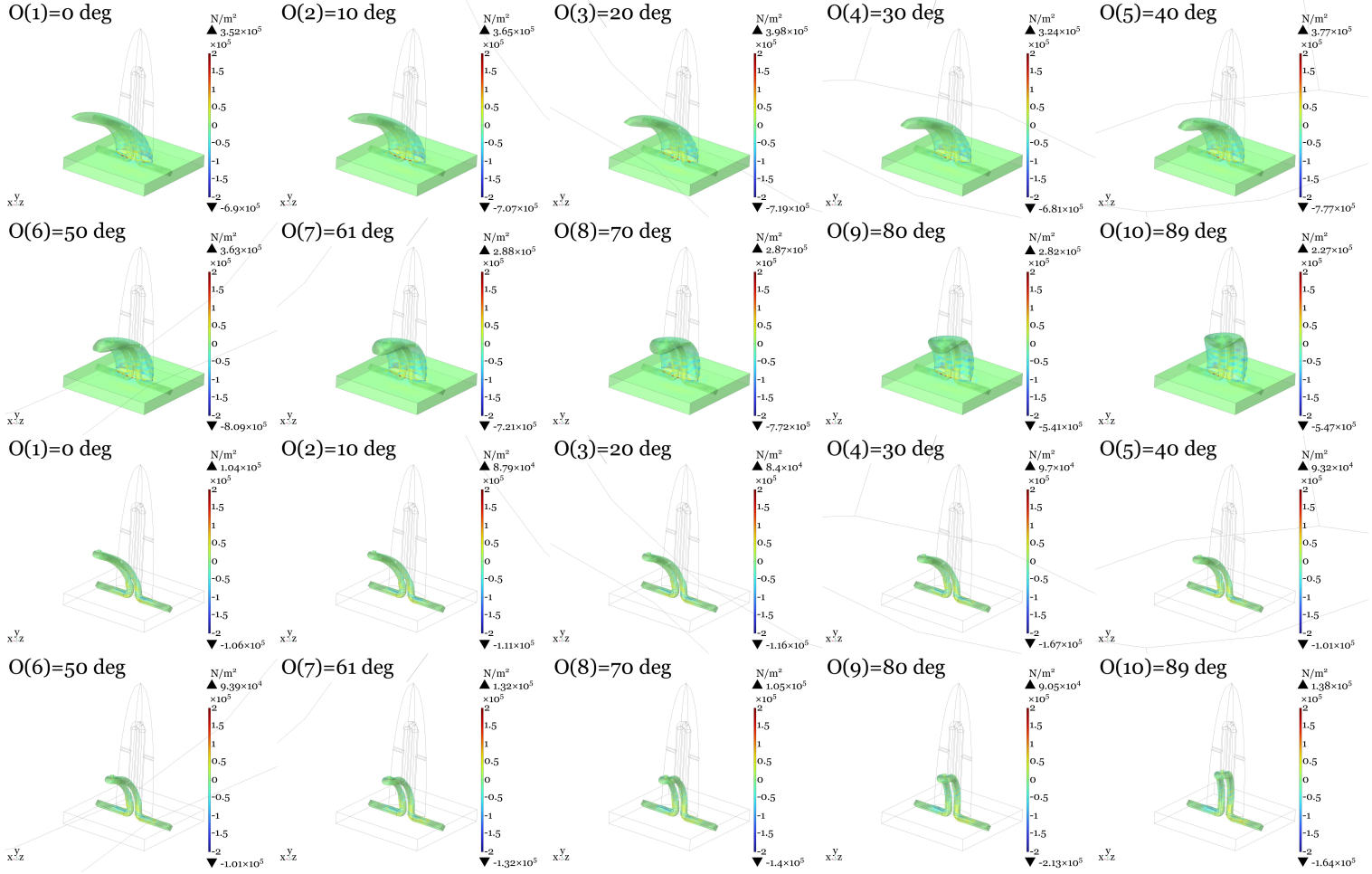

Fig. 25: Stress plot of the cupula and inner tube for all tested flow angles.